ADMET & DMPK **14** (2026) 3536*; doi: https://doi.org/10.5599/admet.3536*

ADMET

Open Access : ISSN : 1848-7718

http://www.pub.iapchem.org/ojs/index.php/admet

Original scientific paper

Anti-amyloid activity of carrageenan-loaded liposomal nanocarriers against subcutaneous insulin-induced amyloid masses in rats

Saranya Udayakumar[1], Koyeli Girigoswami[2], Venkatakrishnan Kiran[1], Devadass Jessy Mercy[1], Vijayashree Raghavan[3] and Agnishwar Girigoswami[1,*]

[1]*Medical Bionanotechnology, Faculty of Allied Health Sciences, Chettinad Hospital & Research Institute (CHRI), Chettinad Academy of Research and Education (CARE), Kelambakkam, Chennai, TN-603103, India*
[2]*Medical Bionanotechnology Lab, Department of Obstetrics and Gynaecology, Saveetha Medical College and Hospital, Saveetha Institute of Medical and Technical Sciences, Thandalam, Chennai, TN-602105, India*
[3]*Department of Pathology, Vels Medical College and Hospital, Manjankaranai, Chennai, TN-601102, India*

Corresponding Author: E-mail: *dragnishwar@care.edu.in; agnishwarg@gmail.com; Tel: +91-44-4742-9046

Received: July 1, 2026; Revised: August 18, 2026; Published: August 20, 2026

Abstract

Background and purpose: Protein misfolding and subsequent amyloid formation are associated with various diseases like localized amyloidosis, type II diabetes, and other neurodegenerative diseases. Insulin can undergo fibrillation under specific physiological conditions, leading to the formation of localized amyloid deposits. Repeated subcutaneous administration of insulin fibrils induces amyloid mass at injection sites. **Experimental approach**: This study investigated the pathological consequences of insulin fibril deposition in a rat model and evaluated the anti-amyloid efficacy of iota-carrageenan (CG) and its liposomal nano-formulation (nCG). Repeated subcutaneous administration of insulin for 28 days induced the formation of a well-defined amyloid mass. **Key results**: Treatment with nCG markedly reduced amyloid accumulation and effectively suppressed amyloid progression. Histopathological examination demonstrated a concentration-dependent reduction in amyloid deposits following CG treatment, while nCG-treated groups exhibited no detectable amyloid accumulation. The formation and inhibition of amyloid were further validated by haematoxylin and eosin (H&E), Congo red and thioflavin T (ThT) staining. In addition, nCG showed excellent biocompatibility, with no observable pathological alterations in major organs. **Conclusion**: Collectively, these findings indicate that both CG and nCG possess significant anti-amyloid activity, with nanoformulated CG showing enhanced efficacy in preventing insulin-induced localized amyloidosis.

Keywords

Localized amyloidosis, neurodegenerative diseases, amyloid clearance, healthcare, sulphated polysaccharide

Introduction

Amyloid formation is a significant pathological feature in several neurodegenerative diseases, including Alzheimer's disease (AD), Parkinson's disease (PD), Type II diabetes, and other forms of amyloidosis [1-3]. In these conditions, soluble proteins undergo conformational changes to form insoluble fibrillar aggregates known as amyloid fibrils [4]. These fibrils are well known for their highly arranged β-sheet-rich structure and typically exhibit thread-like morphology. They can involve toxic intermediates during the self-assembly process [5].

Amyloid fibrils are composed of 2-8 protofilaments, each with a diameter of approximately 7 to 13 nm and a height that ranges from 2-7 nm [6,7]. Amyloid deposition can occur systemically or locally. Localized amyloid tumours are confined deposits that are frequently associated with mild symptoms [8]. These deposits have been observed in conditions such as chronic inflammation, osteomyelitis, haemodialysis, and tuberculosis. In some cases, amyloid deposition occurs in subcutaneous tissues or the gastrointestinal regions [9,10].

A clinically significant type of localized amyloidosis is injection-related amyloidosis, which has been increasingly noted in diabetic patients receiving long-term insulin treatment [11]. Injection amyloidosis arises from repeated subcutaneous insulin administration at the same injection site. Regular injections promote local insulin accumulation, leading to misfolding and aggregation into amyloid fibrils. This localized amyloid mass is commonly referred to as an amyloidoma, an insulin ball, and an insulin-derived localized amyloidosis [12,13]. Numerous clinical studies have demonstrated that insulin injected into amyloid-containing tissue results in reduced, unpredictable absorption, thereby impairing glycaemic control and increasing the risk of hypoglycaemia [14]. To overcome these issues, many patients increase their insulin dosage, which increases amyloid mass accumulation [15,16]. In addition, insulin amyloid (IA) deposits are also associated with inflammation, local tissue stress, and cytotoxic effects on surrounding cells. Therapeutic options for insulin-induced localized amyloidosis remain limited [17]. Currently, surgical excision is considered the only effective treatment. Preventive measures, such as changing injection sites and avoiding the affected area, are used to improve insulin absorption [18, 19]. However, they do not remove existing amyloid deposits [20]. These limitations highlight the urgent need for an alternative treatment approach to reduce insulin amyloid masses. Insulin amyloid fibrils serve as a widely used model system for studying amyloid formation and evaluating anti-amyloid agents for targeting neurodegenerative diseases [21,22].

Various animal studies have established the feasibility of inducing localized insulin amyloidosis. Kheirbakhs *et al*. subcutaneously injected insulin fibrils into the left abdominal region of animals for 12 consecutive days. Turmeric treatment reduced amyloid mass [23]. In another study, human insulin incubated at 57 °C for 24 h formed amyloid fibrils and was subcutaneously injected for 21 days to induce localized deposits in mice [24]. Similarly, amyloid fibrils formed by heating the human insulin at 65 °C were injected subcutaneously for 14 days. The anti-amyloid potential of lumbrokinase and serratopeptidase was studied by attenuating the subcutaneous amyloid mass [25].

These findings suggest that *in vivo* investigation of amyloid degradation can facilitate the identification of therapeutic drugs. Sulphated polysaccharides like carrageenan were studied for their anti-amyloidogenic activity [26]. Nanoformulation offers several advantages, including enhanced stability[27-29], sustained release [30], and increased surface area for interaction with fibrillar aggregates at the injection site. These properties may improve uniform drug distribution on the amyloid mass and increase degradation efficiency by minimizing toxicity. Panda et al. synthesized BDNF-loaded EGCG-dopamine-tryptophan nanoparticles that demonstrated enhanced therapeutic efficacy against Alzheimer's disease by inhibiting Aβ fibrillization, promoting amyloid plaque clearance, reducing oxidative stress, and protecting neuronal cells [31]. Nano-particle-based drug delivery systems offer an effective strategy to overcome blood-brain barrier limitations in Alzheimer's disease by improving drug stability and brain penetration, thereby enhancing therapeutic efficacy and providing a promising platform for the development of advanced AD treatments [32,33]. RVG-NV-NPs, a neural stem cell (NSC) membrane-coated nanoparticle system, were developed by Huang et al. for efficient and traceable CNS drug delivery in Alzheimer's disease [34]. By combining RVG-mediated acetylcholine receptor targeting with the natural brain-homing ability of NSC membranes, the nanoparticles achieved prolonged blood circulation, enhanced blood-brain barrier penetration, and improved neuronal targeting. Encapsulation of bexarotene and AgAuSe quantum dots enabled simultaneous therapy and near-infrared-II

imaging of the delivery process [34]. Therefore, nanoformulations offer an effective strategy for amyloidosis treatment by enhancing targeted delivery, inhibiting amyloid aggregation, promoting plaque clearance, and improving overall therapeutic outcomes.

In our previous study, we investigated the potential effect of nanoformulated iota carrageenan (nCG) to degrade IA and amyloid β (Aβ) [35] fibrils both *in vitro* and *in vivo* using a zebrafish model. Currently, no animal model of localized amyloidosis has been reported to evaluate the anti-amyloid efficacy of nanoformulated carrageenan [36]. In the current investigation, preformed insulin amyloid was administered subcutaneously to rats in both treated and untreated groups. The formation and progression of amyloid deposits were evaluated using haematoxylin and eosin (H&E) staining, Congo red staining, and thioflavin T (ThT) fluorescence imaging with the Lumina (PerkinElmer) live animal imaging system. Excised tissue from the insulin amyloid (IA; G3) group showed clear amyloid deposition, as confirmed by these staining techniques. In contrast, animals treated with nanoformulated carrageenan (nCG) showed a marked reduction in amyloid accumulation, indicating effective attenuation of amyloid deposits. These findings demonstrate the anti-amyloid efficacy of both carrageenan (CG) and nCG in promoting the degradation of localized insulin-induced amyloidosis. Haematological and biochemical analyses were primarily performed to evaluate whether the intervention induced any systemic toxicity. In addition, histological analysis of major organs confirmed the absence of treatment-related pathological alterations and supports that the treatment attenuates the localized mass by maintaining systemic biocompatibility.

Materials and methods

Animals

A total of 42 male Wistar albino rats weighing 200 to 300 g were purchased from TANUVAS, Madhavaram, Chennai. The rats were housed in the CHRI animal house under standard conditions: a 12-hour light/12-hour dark cycle, 50 % humidity, and a temperature of 21±2 °C. All animals were provided with unrestricted access to standard feed and drinking water during the experimental period. Before starting the experiment, three animals were housed in each cage and acclimatized in the animal house for one week. The animals were procured after approval from IAEC (IAEC3/proposal: 171/A. Lr: 133/ Dt: 13.12.2024).

Chemicals used

Iota carrageenan (CG) was procured from Himedia. Huminsulin 30/70 IU 40 (Eli Lilly and Company Pvt Limited), Thioflavin T dye from Sigma, Bovine serum albumin, and phosphate buffer saline were purchased from HiMedia; halothane and BD glide 40 IU/31G insulin syringes were procured from local shops. ImageJ software was used to generate intensity-based heatmaps.

Amyloid preparation

Amyloid fibrillation of Huminsulin was prepared through thermal incubation at 65 °C following a standard protocol [37]. The ThT fluorescence intensity and fluorescence microscopy confirmed the formation of amyloid fibrils. ThT fluorescence was measured using the Jasco-FP8300 model, and an Olympus BX51 fluorescent microscope was used to obtain a morphological image of amyloid fibrils.

Fourier transform infrared spectroscopy analysis

Fourier transform infrared (FTIR) spectra of the IA samples with and without treatment were recorded after baseline correction. The amide I band was observed within the range of 1590-1630 cm^{-1}, indicating the presence of a β-sheet structure. The degradation of IA by nCG was analysed using FTIR spectroscopy by comparing spectra before and after treatment.

Carrageenan and nanoformulated carrageenan preparation

In this experiment, 10 mg of commercially available iota carrageenan (CG) was dissolved in distilled water and heated at 60 °C with continuous magnetic stirring for 30 min. Nanoformulated carrageenan (nCG) was synthesized using a thin-film hydration technique. A liposome was prepared using a phospholipid with NaCl, methanol, and chloroform [38]. The complete mixture was evaporated using a rotary vacuum pump. The thin lipid film was further dried in a desiccator. The film was hydrated and sonicated for 15 min. Following this, 20 mg of CG was encapsulated within the liposomal vesicle by sonicating for 15 min at 20 to 25 °C.

Experimental groups

Based on the *in vitro* toxicity and amyloid degradation experiments in the zebrafish model. Two doses of CG and nCG were chosen for the study. Dose A of CG and nCG (50 mg kg^{-1}) and Dose B of CG and nCG (300 mg kg^{-1}). 42 male Wistar albino rats were divided into seven groups (n=6 in each group) as mentioned below.

The experimental animals were randomly allocated into seven groups to evaluate the therapeutic effects of CG and nCG under normal and IA-induced conditions. Group 1 served as the CG sample control and received 0.9 mL of buffer along with 0.1 mL of dose B of CG, while Group 2 functioned as the nCG sample control and was administered 0.9 mL of buffer and 0.1 mL of dose B of nCG. Group 3 served as the disease control and received 0.9 mL of IA and 0.1 mL of PBS without treatment. Treatment groups included Group 4, which received IA together with a low dose (dose A) of CG, and Group 5, which received IA combined with a high dose (dose B) of CG. Similarly, Group 6 received IA and a low dose (dose A) of nCG, whereas Group 7 received IA with a high dose (dose B) of nCG. This experimental design enabled a comparative assessment of the dose-dependent effects of CG and nCG against IA-induced pathological changes while also including appropriate control groups for accurate evaluation.

Each treatment sample was administered subcutaneously for 28 consecutive days on the left side of the abdomen. During the study period, all animal groups received a normal diet. This study's experimental protocol was designed in compliance with the International Guidelines for the Care and Use of Laboratory Animals (Institute of Laboratory Animal Resources, 1996) and approved by the Institute of Animal Ethics Committee (IAEC) at Chettinad Academy of Research and Education (CARE), Chennai (IAEC3/proposal: 171/A. Lr: 133/ Dt: 13.12.2024).

Histopathological analysis

After 28 days of repeated subcutaneous administration of insulin amyloid (IA) fibrils, an amyloid waxy mass developed in the experimental groups. This amyloid mass was excised and weighed. Major organs (brain, heart, liver, kidney, and spleen) were also collected from all groups to evaluate potential toxic effects. The collected tissues and organs were rinsed three times in 0.9 % saline and stored in 10 % formalin. The waxy mass tissues were then paraffin-embedded, and 5 µm-thick sections were prepared and mounted on glass slides. The sections were stained with haematoxylin and eosin (H&E), Congo red, and PAS and examined under a light microscope at 10× and 40× magnification. Intensity-based colour heatmaps were generated from Congo red-stained histopathological images using ImageJ software. The heatmap facilitates enhanced visualization and interpretation of amyloid deposition. Furthermore, ThT staining was employed to assess amyloid deposition in paraffin-embedded waxy mass tissue sections obtained from groups G1 to G7 using a Lumina small animal *in vivo* imaging system. The extent of amyloid-associated fluorescence was quantitatively analysed by measuring the fluorescence intensity within the selected regions of interest (ROIs).

Haematological parameters

The animals were anesthetized, and the blood samples were collected from the retro-orbital plexus for all experimental groups. The collected blood was immediately transferred into EDTA-coated tubes and stored at

4 °C until analysis. A complete blood count (CBC) was performed, including evaluation of haematological parameters such as red blood cells (RBC), white blood cells (WBC), packed cell volume (PCV), mean corpuscular volume (MCV), mean corpuscular haemoglobin (MCH), haemoglobin, neutrophils, lymphocytes, monocytes, eosinophils, basophils, platelets, mean platelet volume (MPV) and mean corpuscular haemoglobin concentration (MCHC). All analyses were carried out using an EXIGO EOS vet haematology analyser.

2.9. Blood serum biochemical analysis

Blood was collected from the retro-orbital plexus in uncoated EDTA tubes and maintained at room temperature for 1 h. The blood samples were then centrifuged at 4000 rpm for 10 min. Serum was used to analyse various serum proteins, including blood urea nitrogen (BUN), sodium, total protein, albumin, total bilirubin, and uric acid, using the A15 Auto biochemical analyser.

2.10. Statistical analysis

Significant differences between groups were analysed using One-way ANOVA. A *p*-value below 0.05 was deemed statistically significant. The experimental data were expressed as mean ± standard error. The differences between the control and treatments were represented as * - $p < 0.05$, ** - $p < 0.02$, *** - $p < 0.01$, **** - $p < 0.001$. Significant differences between groups were denoted as α - $p < 0.001$, β - $p < 0.01$, γ - $p < 0.02$ and δ - $p < 0.05$.

Result and discussion

Amyloid formation analysis

Thioflavin T (ThT) is a benzothiazole-based fluorescent dye. It exhibits increased fluorescence by binding to insulin amyloid fibrils. In this study, the newly formed insulin amyloid was evaluated using a ThT fluorescence assay after incubating insulin at 65 °C overnight. A significant increase in fluorescence intensity was observed compared to ThT and ThT+BSA. Bovine serum albumin (BSA) was used as a negative control (non-amyloidogenic). The increased fluorescence intensity indicates the formation of a characteristic cross-β sheet structure, as depicted in Figure 1A.

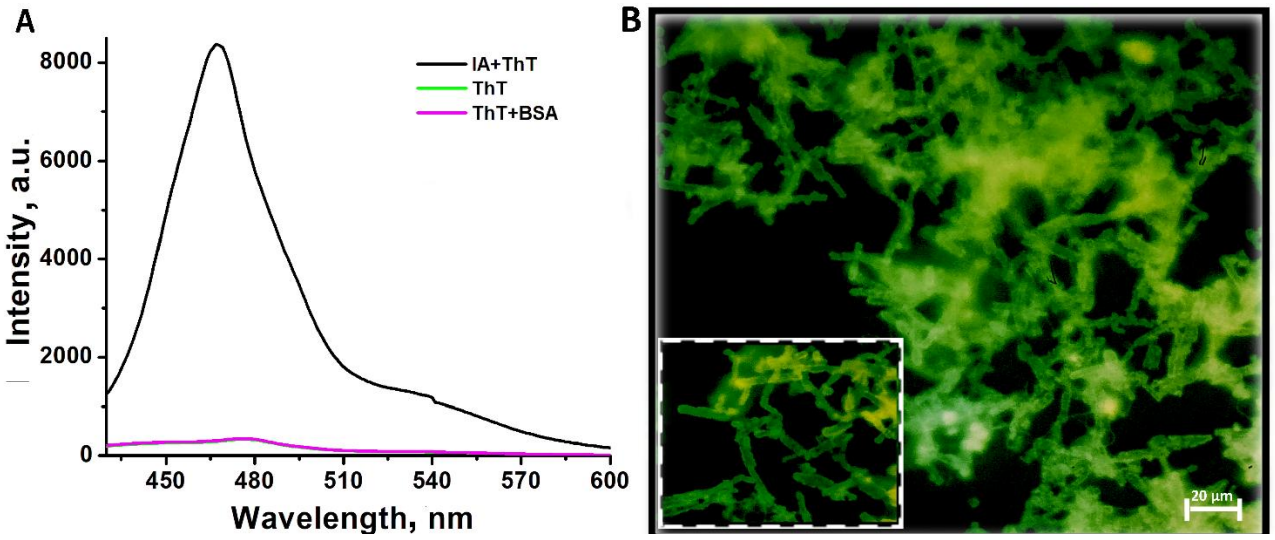

Figure 1. Confirmation of insulin amyloid formation by thioflavin T fluorescence analysis. (A) ThT-fluorescence assay demonstrates the formation of insulin amyloid fibrils. A significant increase in fluorescence intensity confirms the conversion of soluble insulin into β-sheet-rich amyloid aggregates. The enhanced fluorescence indicates the specific binding of ThT dye to IA (black). ThT alone (green) and ThT+BSA (pink) exhibited minimal fluorescence, indicating the absence of amyloid structure. (B) Fluorescence microscopic image of IA stained with ThT showing bright green fluorescence

The morphological structure of the amyloid fibrils was examined using fluorescence microscopy. ThT dye bound to IA showed bright yellow-green fluorescence with distinct fibrillar morphology, which further confirms the mature IA formation (Figure 1B).

Fourier transform infrared spectra analysis

FTIR analysis was conducted to assess structural modifications in preformed IA alone and in IA treated with nCG. The untreated IA exhibited a prominent peak at 1629 cm^{-1}, confirming a β-sheet-rich secondary structure in the amide I region (Figure 2A). IA treated with nCG showed a peak shift to 1657 cm^{-1} with a lower intensity, indicating a reduction in β-sheets (Figure 2B). This reduction in β-sheet content provides strong evidence supporting the anti-amyloidogenic potential of nCG.

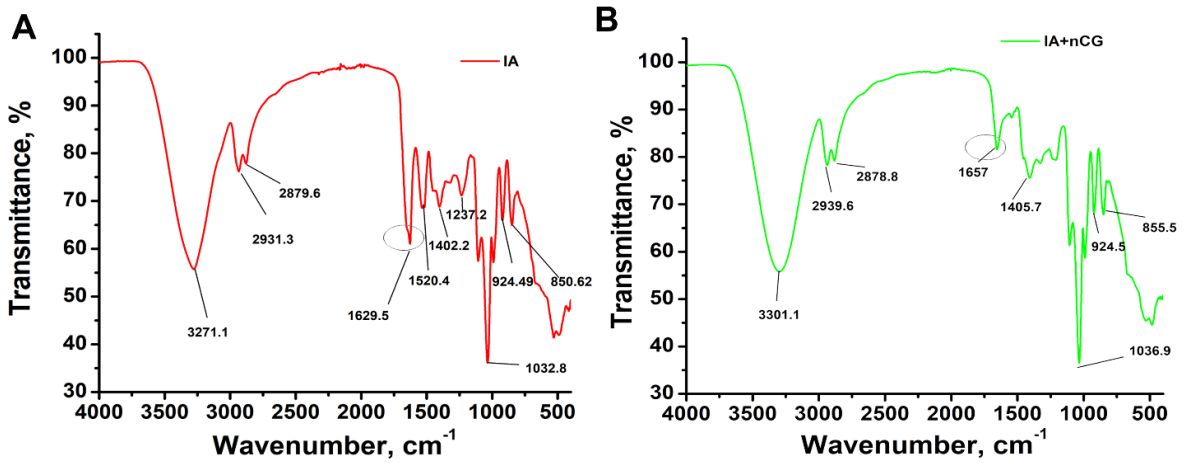

Figure 2. FTIR spectra of IA before and after degradation by nCG. (A) FTIR spectrum of IA showing characteristic absorption peaks corresponding to the β-sheet structure of amyloid. (B) FTIR spectrum of IA after degradation by nCG showing the alterations in peak intensity, shifting of functional groups, and indicating β-sheet structural reduction of IA after being treated with nCG

Morphological investigation of amyloid mass

A distinct waxy amyloid mass developed at the left abdominal injection site after repeated subcutaneous injection. The growth of the amyloid mass was photographed on days 14 and 28, depicted in Figure 3. At day 14, the G3 group showed a prominent waxy mass, as reported by Metkar *et al* [25]. The groups treated with CG and nCG showed a smaller mass, indicating that treatments reduced amyloid formation at an early stage.

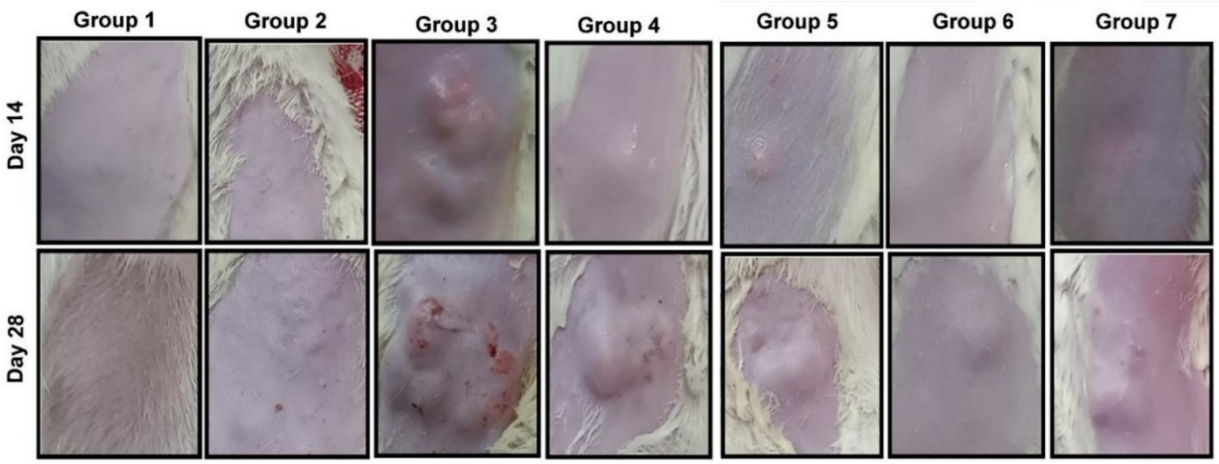

Figure 3. Representative images of the injection site of rats on day 14 and day 28. The images illustrate the comparative progression and regression of IA deposition among the experimental groups for 28 consecutive days. On day 14, the IA deposition was observed at the injection site in G3, G4, and G5. On day 28, the untreated IA group showed further enlargement of the amyloid mass in G3. In contrast, the treated groups showed a noticeable reduction in amyloid mass size, indicating the anti-amyloidogenic effect of the treatment

By day 28, the IA-injected animals showed increased mass size. However, the treated groups showed reduced mass size. Among them, the nCG-treated group showed better improvement than the CG-treated group, with a smaller mass size.

After 28 days, the masses were excised and weighed to evaluate amyloid degradation. Two different doses of CG and nCG (50 mg/kg and 300 mg/kg) were tested. Morphological observation revealed a large amyloid mass in the untreated IA group, whereas treatment with CG and nCG resulted in a reduction in the mass size (Figure 4A). The excised masses were weighed, showing that CG reduced the amyloid mass by up to 36.9% and 43%, and nCG showed a greater reduction of 74% and 77.7% at Dose A and Dose B, respectively (Figures 4B and C). Treatment with CG (300 mg/kg) showed a decrease compared to the IA untreated positive control. Notably, treatment with nCG exhibited a statistically significant reduction ($p<0.001$) in subcutaneous amyloid mass compared to both the IA and IA+CG groups. Both morphological assessment and excised tissue weight results confirmed nCG's distinct inhibitory effect on subcutaneous amyloid deposition.

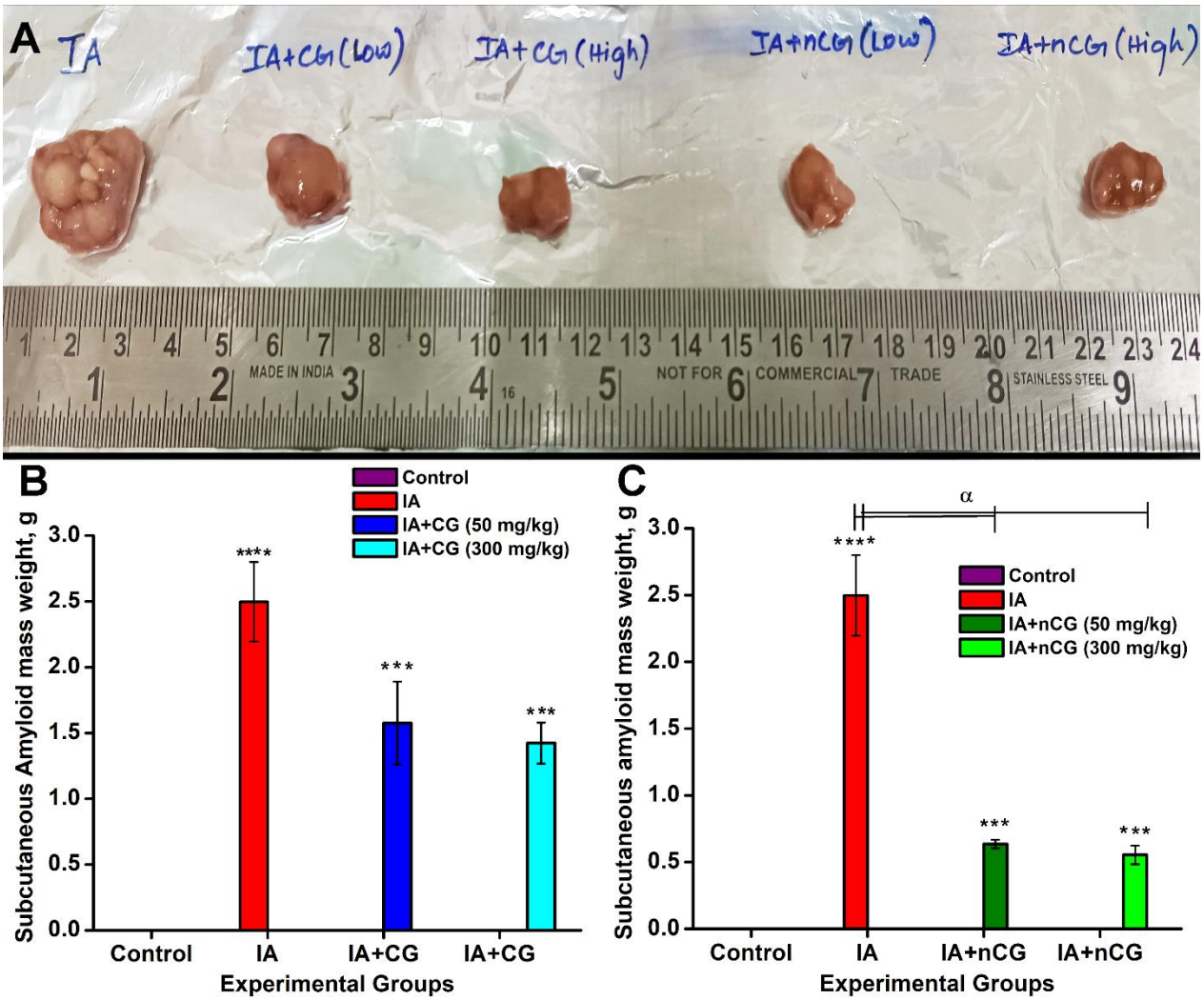

Figure 4. The weight of subcutaneously formed masses were compared between the groups: (A) morphological image of the excised amyloid mass (B) comparison between IA (untreated which received IA fibrils), IA+CG (which received IA fibrils and 50 mg kg-1, 300 mg kg^{-1} of CG), (C) IA (untreated which received IA fibrils), IA+nCG (which recived IA fibrils and 50, 300 mg kg^{-1} of nCG). Significant differences between control groups are represented as ***p <0.01, **** p<0.001, and between groups as α - p <0.001

Monitoring of body weight, feed, and water intake

Body weight, feed, and water intake of all experimental groups were monitored throughout the 28-day study period (Supplementary material, Tables S1, S2, and S3). Body weight in the G1 and G2 groups increased

gradually from day 1 to 28. A similar increase in body weight was also observed in the IA-injected groups. A significant variation was noted in the IA-injected group compared with the other treatment groups. Feed intake in the G3 (IA) was comparable to that of the other groups on day 1. After 7 days of injection, feed intake decreased significantly compared to groups G5 to G7. In the groups treated with CG and nCG, water consumption remained similar to that of other groups, whereas the IA-injected groups showed lower water intake by day 28. Overall, the findings show that although feed intake decreased after IA injection, body weight continued to increase, indicating the accumulation of localized amyloid deposits in the abdominal region.

Histopathological observation

Localized amyloid deposition and its degradation were examined histopathologically using H&E staining, Congo red, periodic acid-Schiff (PAS), and ThT staining. H&E staining of the IA group (G3) showed prominent amorphous eosinophilic deposits in the subcutaneous tissue, with significant inflammatory cell infiltration, focal necrosis, and sporadic multinucleated giant cells surrounding the deposits, confirming the localized amyloid accumulation (Figure 5A). G4 and G5 (IA+CG) treated groups exhibited eosinophilic deposition and necrosis in the cutaneous layer. In G4 (Figure 6A) and G5 (Figure 6B) groups, the presence of necrotic regions and eosinophilic deposits was shown. However, these changes were notably reduced compared to the G3 group. This reduction indicates partial amyloid degradation. Similarly, the IA+nCG-Treated (Figure 6C and 6D) showed minimal necrosis and no eosinophilic deposits. Hence, these data altogether confirm the degradation effect of nCG. In both the G1 and G2 groups treated with CG and nCG, normal tissue morphology was observed. A mild inflammatory response was observed at the CG-treated injection site and reduced inflammation in the nCG treatment, suggesting that the nanoformulated drug effectively minimized the inflammatory response associated with native CG. Figure S1, Supplementary material, shows the H&E-stained sections of rats injected with CG and nCG via subcutaneous injection. Amyloid deposition was then validated by Congo red staining, a gold-standard technique for amyloid detection. Figure 5C depicts the formation of amyloid in the excised tissue. Positive staining was noted in IA and IA+CG (G4) groups, whereas the nCG-treated groups (Figure 7E and 7G) did not show any positivity for Congo red staining. To visualize clearer positive amyloid regions, heatmaps were generated. Amyloid-positive regions were distinctly highlighted in yellow, whereas non-amyloid tissue regions appeared in purple (Figure 5D). The amyloid-deposited area was 80.71% in G3. The CG-treated groups (Figure 7B and D) exhibited prominent yellow areas, indicating persistent amyloid deposits within the tissue sections. G4 and G5 showed 71.29 and 68.73 % amyloid, indicating dose-dependent attenuation. Comparatively, the nCG-treated groups (Figure 7F and H) showed no detectable yellow regions, suggesting effective attenuation and clearance of amyloid deposition following treatment. The localized amyloid IA showed negative PAS staining (Figure 5B), which corroborated the deposition of amyloid in the cutaneous layer. Previous studies have also reported similar findings, highlighting the amyloid-reducing effectiveness of turmeric [23]. Additionally, our previous study using lumbrokinase and serratiopeptidase demonstrated antiamyloid activity by reducing amyloid formation in a rat model [25]. Histopathological analysis of major organs showed various alterations among the groups. In CG- and nCG-treated animals, mild congestion and inflammation were noticed in the kidney, and other organs remained normal. In the IA-treated groups, the kidneys showed tubular damage and coagulative necrosis, and the spleen showed significant congestion. IA+CG (G4) showed renal congestion with inflammatory changes in the spleen. In G5, splenic congestion was observed with inflammation in the liver. The G6 group showed slight congestion, while the remaining organs appeared normal. In G7, no detectable abnormalities in any of the examined organs, as presented in Figure S2.

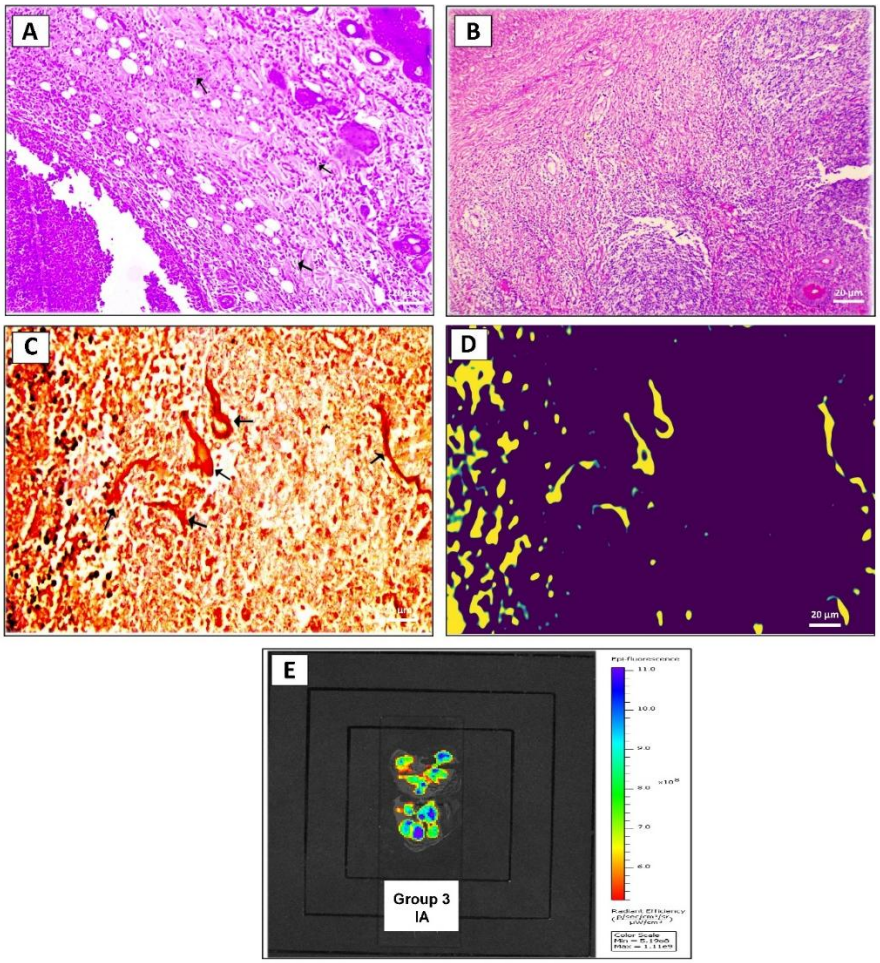

Figure 5. Histopathological observation of subcutaneous amyloid mass in the IA-induced group (G3). (A) H&E-stained section showing eosinophilic deposits. (B) PAS-stained section showing PAS-negative. (C) Congo red-stained section viewed under bright-field microscopy demonstrating characteristic amyloid deposits within the subcutaneous tissue. (D) Intensity-based heatmap representation of a Congo red-stained histopathological section showing separation of amyloid and non-amyloid regions. (E) ThT-stained pathology slides visualized using an *in vivo* imaging system. They show enhanced intensity corresponding to amyloid deposition. Arrows highlight eosinophilic and amyloid deposits in the subcutaneous layer

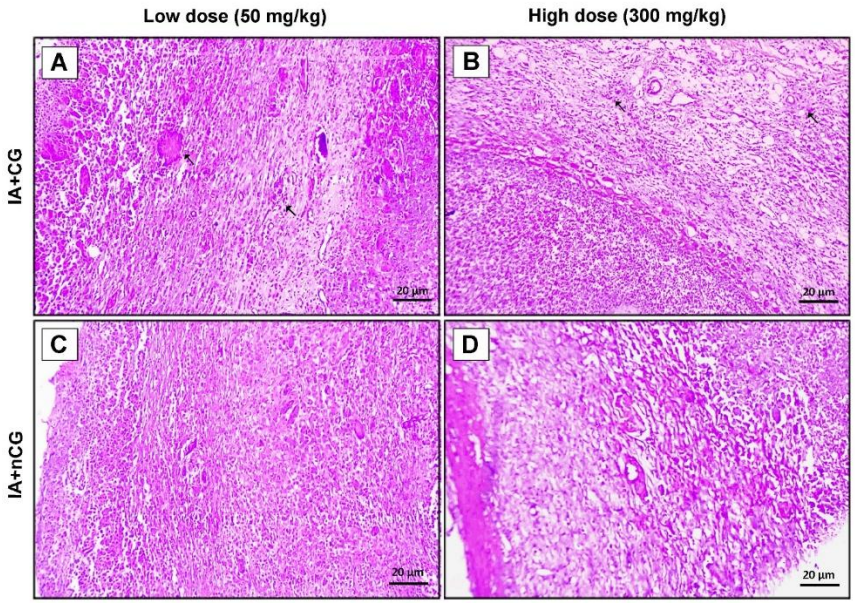

Figure 6. H&E-stained sections of abdominal subcutaneous amyloid mass from treatment groups. (A) IA-treated with CG low dose. (B) IA-treated with CG high dose. (C) IA-treated with nCG low dose. (D) IA-treated with nCG high dose. Arrows indicate eosinophilic deposits within the subcutaneous tissue section

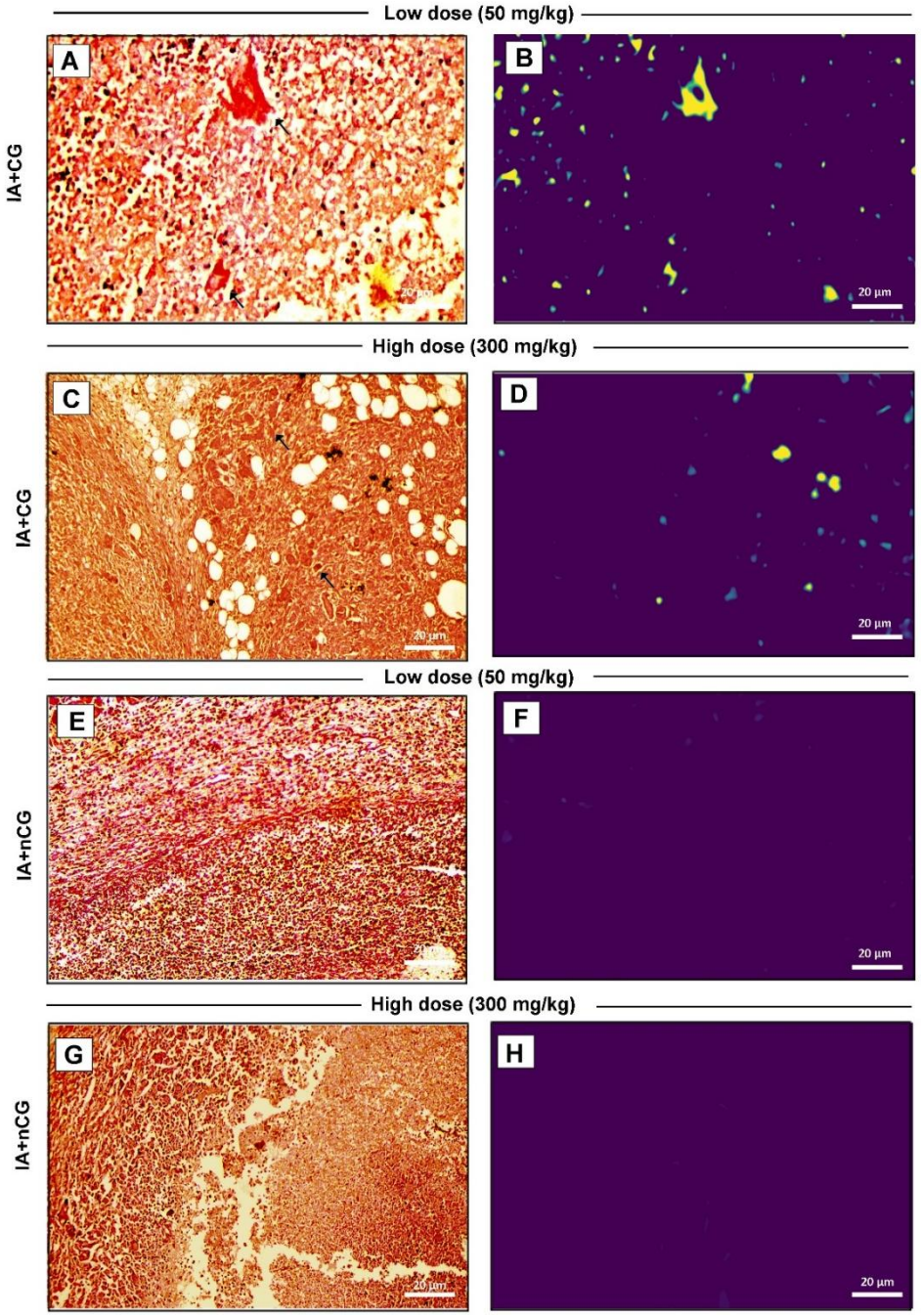

Figure 7. Congo red-stained sections of abdominal subcutaneous mass from treatment groups. (A) IA-treated with CG low dose. (B) Intensity-based heatmap analysis of Congo red-stained IA+CG samples revealed the presence of amyloid-positive regions with moderate fluorescence intensity. (C) IA treated with CG high dose. IA treated with CG confirmed the presence of amyloid deposits within the tissue, observed as red-stained regions under bright-field microscopy. (D) Intensity-based heatmap analysis of Congo red-stained IA+CG (high dose). (E) IA treated with low-dose nCG, (F) Intensity-based heatmap analysis of Congo red-stained IA+nCG (low dose). (G) IA treated with high-dose nCG. (H) Intensity-based heatmap analysis of Congo red-stained IA+nCG (high dose). IA treated with nCG comparatively showed no visible red-stained region, indicating the antiamyloidogenic effect of the treatments on amyloid deposits. Amyloid-positive (red regions) are indicated by black arrows

Thioflavin T staining

ThT-stained pathological sections in slides were used to assess amyloid presence at the injection site. Strong fluorescence was observed in the IA group (Figure 5E and 8C), confirming the amyloid deposition. G4 and G5 (Figures 8D and 8E) showed reduced fluorescence intensity, which indicates partial degradation. No significant fluorescence was detected in G6 and G7 (Figure 8F and 8G), suggesting effective amyloid degradation. Similarly, G1 and G2 showed no fluorescence, confirming the specificity of the ThT binding to

amyloid deposits. Quantitative analysis of fluorescence intensity was performed using the ROI tool in the Lumina *in vivo* imaging system, depicted in Figure 9. These findings confirm the aforementioned results and show that both nCG doses reduced amyloid mass.

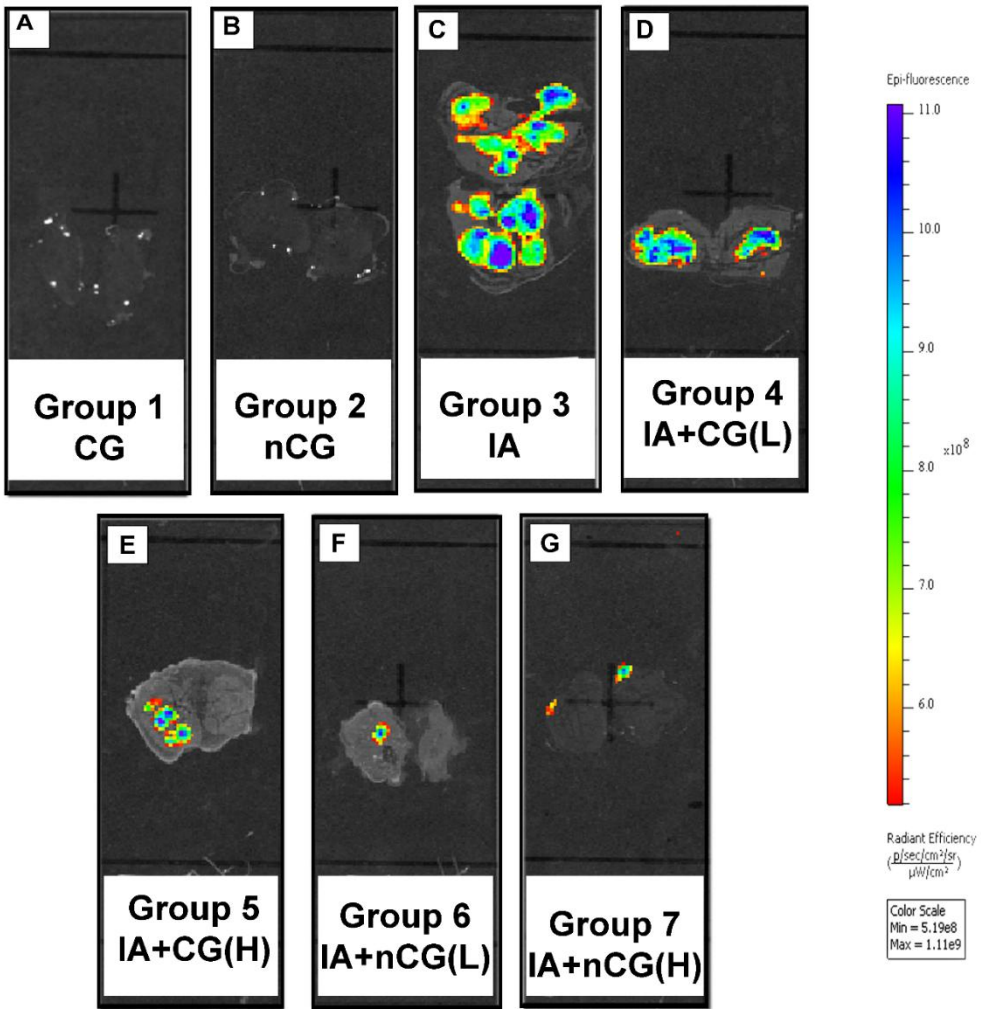

Figure 8. Histopathological slides stained with ThT and visualized using an *in vivo* imaging system exhibited fluorescence signals at localized amyloid deposits on the abdominal subcutaneous mass. (A) G1 received CG, (B) G2 received nCG and both groups showed no detectable fluorescence due to the absence of amyloid deposits. (C) G3 received IA, exhibited intense fluorescence, indicating significant amyloid accumulation in the subcutaneous layer. (D) G4 received IA and Dose A of CG, (E) G5 received IA and Dose B of CG, showing comparatively reduced fluorescence intensity. (F) G6 received IA and Dose A of nCG, (G) G7 received IA and Dose B of nCG, showing minimal fluorescence, suggesting the amyloid degradation effect of nCG

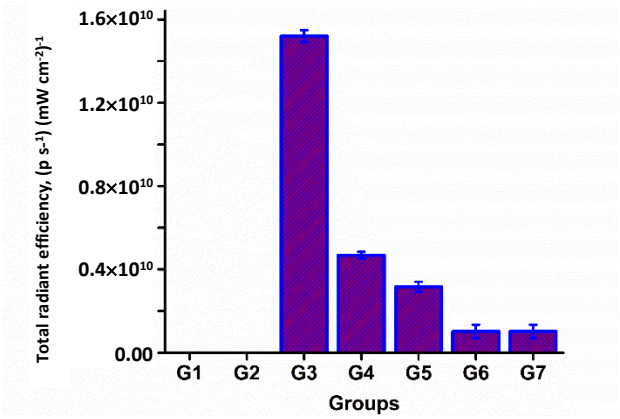

Figure 9. ROI fluorescence values of ThT-stained pathology slides obtained by the *in vivo* imaging system. Increased fluorescence intensity corresponds to higher amyloid accumulation, while treatment groups showed reduced ROI fluorescence values compared with the untreated IA group, indicating decreased amyloid deposition after treatment

Hematological parameters

Haematological parameters, including RBC, WBC, PCV, MCV, MCH, haemoglobin, neutrophils, lymphocytes, monocytes, eosinophils, basophils, platelets, MPV and MCHC, were analysed across all experimental groups (Table 1). Most parameters were within normal physiological ranges, except PCV and platelets, indicating that localized subcutaneous amyloid deposition did not lead to systemic amyloidosis. PCV differed significantly between the IA and nCG-treated groups (p <0.001), with additional variations in the CG and nCG-treated groups compared with the control. Furthermore, there was a significant difference (p <0.05) between the IA and IA+nCG (Dose B) groups. Platelet counts showed statistically significant changes (p <0.001) in both the IA and treated groups. Basophils were absent in all groups. The alteration in PCV and platelet counts may be due to a localized inflammatory response. It may also result in local amyloid buildup, which can trigger localized inflammatory responses associated with amyloid deposition and influence haematopoiesis and platelet activation.

Table 1. Haematological parameters of different treatment groups were analysed. Values are expressed as mean ± standard error. α - p <0.001 represents the significant differences between the groups

Groups	CG	nCG	IA	IA+CG		IA+nCG	
	300 mg kg^{-1}	300 mg kg^{-1}		50 mg kg^{-1}	300 mg kg^{-1}	50 mg kg^{-1}	300 mg kg^{-1}
Haemoglobin	11.6±1.0	12.95±0.55	11.7±0.2	11.48±2.32	11.3±1.2	12.55±0.55	11.6±1
RBC	8.41±1.01	9±0.8	9.235±1.3	8.86±1.26	8.93±0.93	9.47±2.5	8.4±1.3
WBC	7.71±1.71	8.03±0.63	11.405±2.6	13.03±0.03	10.67±0.37	8.8±2	8.96±2.86
Platelets count	1097.5±5$^{\alpha}$	1159±47$^{\alpha}$	1013.5±53$^{\alpha}$	1165±85$^{\alpha}$	1098±62	1052±44$^{\beta}$	1045.5±34.5$^{\delta}$
PCV	345.25±290.75$^{\alpha}$	53.2±5$^{\alpha}$	52.2±13.2$^{\alpha}$	52.45±12.35	49.75±8.35	45.2±5.4	48.65±10
MCV	55.7±5.3	57.1 ± 5.3	54.15±7.75	52.5±2.8	51.35±7.55	47.1±6	50.65±10
MCH	12.45±2.25	13.85±1.25	12.85±1.95	13.7±2.6	12.65±2.35	13.8±1.9	13.75±2.75
Neutrophils	25±5	42.5 ± 18.5	35±7	31.5±8.5	29.5±8.5	32±11	25.5±3.5
Lymphocytes	71.5 ± 3.5	53 ± 16	59±6	63.5±6.5	67±8	65.5±9.5	66±6
Monocytes	2.5±0.5	3.5±1.5	3.5±0.5	3.5±1.5	3±0	2±1	2.5±1.5
Eosinophils	1±1	1±1	2±1	1.5±0.5	0.5±0.5	0.5±0.5	1±1
Basophils	-	-	-	-	-	-	-
MCHC	16.15±0.55	19.5±2.8	17.85±0.35	19.9±1.7	21.6±4.2	22.85±4.35	22.2±4.2
MPV	7.55±0.45	7.4±0.3	7.2±0.3	7.5±0	7.75±0.35	7.9±0.1	7.35±0.35

Serum biochemical parameter analysis

The biochemical parameters across all experimental groups are shown in Figure 10. The analyzed markers included BUN, sodium, total protein, albumin, blood urea nitrogen, total bilirubin, and uric acid. Among these, BUN levels were increased in the G6 and G7 groups, showing a significant difference (p <0.05). Uric acid exhibited a significant difference between the G3 and all treatment groups (p <0.001). Sodium levels also showed notable variation (p <0.001). Overall, the observed changes in BUN, sodium, and uric acid, and no notable alterations were detected in other biochemical parameters. These findings indicate that localized amyloid deposition and subsequent treatment do not lead to systemic toxicity.

Amyloid deposition in the subcutaneous layer leads to the development of localized amyloidosis [39,40]. A prominent type of localized amyloidosis is observed at insulin injection sites among diabetic patients. Since the initial documentation of insulin-induced localized amyloidosis in 1983, numerous studies have explored the pathological characteristics and development of insulin-related amyloid accumulation in both human and experimental animal models. A previous study by Chinisaz *et al.* [24] showed that repeated subcutaneous injection of insulin amyloid for 21 consecutive days led to the formation of localized amyloid deposits in mice. Similarly, the repeated injection in rats resulted in the development of amyloid mass, while treatment with turmeric notably reduced the size of amyloid and modified tissue structure [23]. Azarfar *et al*. reported that silymarin reduced amyloid deposition and inflammatory markers such as MMP2, TNF-α, and IL-6 in localized insulin-derived amyloidosis in a rat model [9].

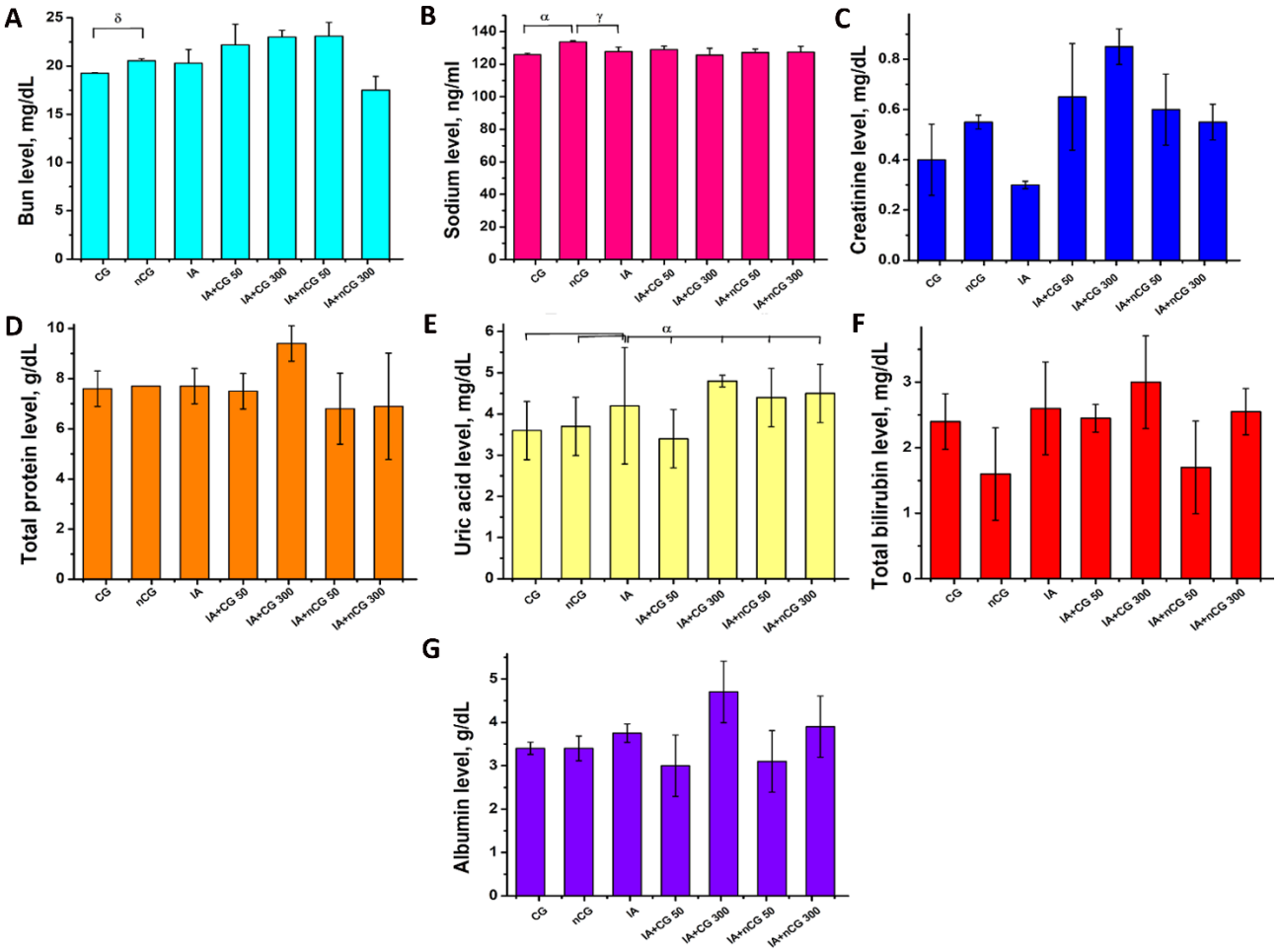

Figure 10. Biochemical levels of animals treated with different experimental groups. (A) BUN, (B) sodium, (C) creatinine, (D) total protein, (E) uric acid, (F) total bilirubin, (G) albumin. Statistical significance within the groups was represented as δ - p <0.05, γ - p <0.02 and α - p <0.001

Oleanolic acid exhibited antioxidant and anti-Alzheimer's properties by reducing oxidative stress and inhibiting Aβ1-42 aggregation [41]. These findings highlight the potential of insulin-derived localized amyloidosis models for exploring antiamyloid therapeutic agents. Zhang et al. reported that low-molecular-weight λ-carrageenan enhanced cognitive function and reduced amyloid-related pathology in rats induced with AD [42]. K-carrageenan oligosaccharides decreased Aβ1-42 deposition and mitigated inflammation by inhibiting microglial activation in APP/PS1 transgenic mice [43]. The CG liposomes loaded with homotaurine effectively inhibited the aggregation of amyloid peptide [44].

CG has shown promising antiamyloid activity in ND models; however, few studies have explored its impact on localized insulin-derived amyloidosis. In the present study, insulin amyloid was injected over 28 consecutive days, resulting in localized amyloid masses confirmed by increased size and histopathological staining. Compared with the untreated group IA (G3), the CG- and nCG-treated groups significantly reduced localized amyloid deposition; nCG (300 mg kg^{-1}) showed an excellent inhibitory effect. Previous *in vitro* findings from our work demonstrated that nCG effectively inhibited amyloid, and the present *in vivo* observation on localized amyloidosis further supports these results. Currently, the treatment of localized amyloidosis primarily depends on the surgical removal of insulin mass and avoidance of injection sites. Therefore, these results indicate that nCG could be a therapeutic option for localized insulin amyloidosis. The experimental model used in this research may provide a valuable platform for assessing new antiamyloid agents under physiological conditions.

Conclusion

The current study extends our previous research using a zebrafish model, in which administration of CG and nCG resulted in a significant reduction in insulin amyloid fibrils within 2 h of injection. In that particular study, insulin amyloids were co-injected with a marine source, and amyloid degradation was measured without allowing the development of a localized amyloid mass within the organism. To better mimic the pathological progression of localized amyloidosis, the current study was extended to an *in vivo* rat model. The insulin amyloid mass was developed prior to therapeutic intervention. This method made it possible to assess the amyloid degradation efficacy of CG and nCG on pre-existing amyloid deposits. This physiologically relevant evaluation of the nanoformulation supports its use in reducing localized amyloidosis and suggests its application for clearing accumulation in other tissues. The histopathological observation of amyloid mass sections further supported these findings. In the experimental groups treated with nCG, H&E staining revealed no detectable amyloid degradation, while Congo red staining was negative in treated samples and positive for amyloid deposits in IA. The presence of amyloid deposits was confirmed by groups that had insulin amyloid mass and showed a prominent eosinophilic appearance in H&E-stained sections.

Abbreviations

AD - Alzheimer's disease
PD - Parkinson's disease
IA - amyloid fibrils
Aβ - amyloid β fibrils
H&E - haematoxylin and eosin
ThT - thioflavin T dye,
CG - iota carrageenan
NCG - nanoformulated iota carrageenan
G1-G7 - group 1 to 7
CRC - complete blood count
RBC - red blood cells
WBC - white blood cells
PCV - packed cell volume
MCV - mean corpuscular volume
MCH - mean corpuscular haemoglobin
MPV - mean platelet volume
MCHC - mean corpuscular haemoglobin concentration
PAS - periodic acid-Schiff
ROI - region of interest

Supplementary material

Additional data are available at https://pub.iapchem.org/ojs/index.php/admet/article/view/3536, or from the corresponding author on request.

Author's contribution: *Saranya Udayakumar: Conceptualization, data curation, formal analysis, methodology, writing-original draft preparation; Koyeli Girigoswami: Conceptualization, data curation, methodology, validation, writing-review & editing; Venkatakrishnan Kiran: Methodology, data curation, visualization; Devadass Jessy Mercy: Methodology, data curation, visualization; Vijayashree Raghavan: Methodology, data curation, validation; Agnishwar Girigoswami: Conceptualization, data curation, formal analysis, validation, supervision, project administration, writing-review & editing.*

Conflict of interest: *The authors have no conflict of interest to declare.*

Data availability statement: *All data are included in the manuscript and the supplementary documents.*

Acknowledgement: *The authors are thankful to CARE for infrastructural support. SU, DJM and VK acknowledge CARE for the research fellowship.*

Funding: *No external funding was received.*

References

[1] J.N. Buxbaum, D.S. Eisenberg, M. Fändrich, E.D. McPhail, G. Merlini, M.J.M. Saraiva, Y. Sekijima, P. Westermark. Amyloid nomenclature 2024: update, novel proteins, and recommendations by the International Society of Amyloidosis (ISA) Nomenclature Committee. *Amyloid* **31** (2024) 249-256. https://doi.org/10.1080/13506129.2024.2405948

[2] N. Pathak, S.K. Vimal, I. Tandon, L. Agrawal, C. Hongyi, S. Bhattacharyya. Neurodegenerative disorders of alzheimer, parkinsonism, amyotrophic lateral sclerosis and multiple sclerosis: an early

diagnostic approach for precision treatment. *Metabolic Brain Disease* **37** (2022) 67-104. https://doi.org/10.1007/s11011-021-00800-w

[3] J. Wang, L. Dai, Z. Zhang. Protein aggregation in neurodegenerative diseases. *Chinese Medical Journal* **138** (2025) 2753-2768. https://doi.org/10.1097/CM9.0000000000003802

[4] T. Sinnige. Molecular mechanisms of amyloid formation in living systems. *Chemical Science* **13** (2022) 7080-7097. https://doi.org/10.1039/D2SC01278B

[5] Z. Niu, X. Gui, S. Feng, B. Reif. Aggregation Mechanisms and Molecular Structures of Amyloid-β in Alzheimer's Disease. *Chemistry - A European Journal* **30** (2024) e202400277. https://doi.org/10.1002/chem.202400277

[6] A. Bigi, R. Cascella, F. Chiti, C. Cecchi. Amyloid fibrils act as a reservoir of soluble oligomers, the main culprits in protein deposition diseases. *Bioessays* **44** (2022) 2200086. https://doi.org/10.1002/bies.202200086

[7] F.S. Ruggeri, F. Benedetti, T.P.J. Knowles, H.A. Lashuel, S. Sekatskii, G. Dietler. Identification and nanomechanical characterization of the fundamental single-strand protofilaments of amyloid α-synuclein fibrils. *Proceedings of the National Academy of Sciences* **115** (2018) 7230-7235. https://doi.org/10.1073/pnas.1721220115

[8] P. Shah, C.D. Lee, W. Jin Jeon, A. Dermarderosian, D. Tai, K. Latif, M. Akhtari. The Story of Localized Amyloidosis: Something Old and Something New - A Case Series. *Journal of Investigative Medicine High Impact Case Reports* **13** (2025) 23247096251400068. https://doi.org/10.1177/23247096251400068

[9] K. Azarfar, P. Yaghmaei, M.M. Amoli, N. Hayati-Roodbari, A. Ebrahim-Habibi. Local Insulin-Derived Amyloidosis Model Confronted with Silymarin: Histological Insights and Gene Expression of MMP, TNF-α, and IL-6. *International Journal of Molecular Sciences* **23** (2022) 4952. https://doi.org/10.3390/ijms23094952

[10] M. Pozzan, C. Indennidate, G.G. Varrà, G. Sinagra, M. Merlo, L. Pagura. Amyloidosis and amyloidogenesis: one name, many diseases. *Heart Failure Clinics* **20** (2024) 249-260. https://doi.org/10.1016/j.hfc.2024.02.001

[11] J. Hrudka, E. Sticová, M. Krbcová, K. Schwarzmannová. Localized Insulin-Derived Amyloidosis in Diabetes Mellitus Type 1 Patient: A Case Report. *Diagnostics (Basel)* **13** (2023) 2415. https://doi.org/10.3390/diagnostics13142415

[12] C. Samlaska, S. Reber, T. Murry. Insulin-derived amyloidosis: The insulin ball, amyloidoma. *JAAD Case Rep* **6** (2020) 351-353. https://doi.org/10.1016/j.jdcr.2020.02.011

[13] D. Duong, T. Westhoff-Pankratz, A. Frugoli, S. Pajuleras, K. Ta, B. Barrows, B.D. Barrows. Amyloidoma: a case report of remote insulin-derived amyloidosis in the setting of insulin-dependent diabetes. *Cureus* **16** (2024) e63525. https://doi.org/10.7759/cureus.63525

[14] Y. Shikama, J.-I. Kitazawa, N. Yagihashi, O. Uehara, Y. Murata, N. Yajima, R. Wada, S. Yagihashi. Localized Amyloidosis at the Site of Repeated Insulin Injection in a Diabetic Patient. *Internal medicine (Tokyo, Japan)* **49** (2010) 397-401. https://doi.org/10.2169/internalmedicine.49.2633

[15] S. Amniouel, J. Suh, W. Zheng, Q. Zhang. Beyond amyloid: Nanobody-mediated neuroinflammatory therapy for Alzheimer's disease. *Translational Neurodegeneration* **14** (2025) 51. https://doi.org/10.1186/s40035-025-00513-5

[16] T. Asaithambi, N.S. Bandhakavi, P. Arikrishnan, S. Sridharan, S. Ullas, S. Udayakumar, A. Girigoswami, K. Girigoswami. Spectrofluorimetric Analysis of Amyloid Degradation Using Shankhapushpi Extract/Zinc Oxide Nanoflower—An In Vitro Study. *Chemistry* **8** (2026) 98. https://doi.org/10.3390/chemistry8070098

[17] E. Blázquez, V. Hurtado-Carneiro, Y. LeBaut-Ayuso, E. Velázquez, L. García-García, F. Gómez-Oliver, Juan M. Ruiz-Albusac, J. Ávila, M.Á. Pozo. Significance of Brain Glucose Hypometabolism, Altered Insulin Signal Transduction, and Insulin Resistance in Several Neurological Diseases. *Frontiers in Endocrinology* **Volume 13** (2022) 873301. https://doi.org/10.3389/fendo.2022.873301

[18] A. Das, M. Shah, I. Saraogi. Molecular Aspects of Insulin Aggregation and Various Therapeutic Interventions. *ACS Bio & Med Chem Au* **2** (2022) 205-221. https://doi.org/10.1021/acsbiomedchemau.1c00054

[19] N.M. George, P.M. Sangolli, A. Thulaseedharan, S. Dominic. Cutaneous adverse drug reactions to antidiabetic medications and medical devices used in management of diabetes mellitus. *Journal of Skin and Stem Cell* **11** (2024) e146625. https://doi.org/10.5812/jssc-146625

[20] A. Smith, K. Moore, P. Ambs, A. Saraswati, J. Fortin. Recent Advances in the Discovery of Therapeutics to Curtail Islet Amyloid Polypeptide Aggregation for Type 2 Diabetes Treatment. *Advanced Biology* **6** (2022) 2101301. https://doi.org/10.1002/adbi.202101301

[21] P. Derashri, S. Kadam, J. Lakkakula, S. Barage, A. Roy, K. Kaur, S. Rustagi, D. Verma, S. Raj, S. Malik. Neuroimaging: mapping and diagnosis of neurodegenerative diseases. *Journal of Integrated Science and Technology* **12** (2024) 827-827. https://doi.org/10.62110/sciencein.jist.2024.v12.827

[22] K. Ramasamy, K.P. Gayathri, B.V. Cheriyan, I.G. Josephine, V.D. Deepti. Evaluation of the Neuroprotective Effect of Lawsonia inermis Flower Extract in Alzheimer's Disease-induced Zebrafish Model. *World Journal of Traditional Chinese Medicine* **10** (2024) 451-459. https://doi.org/10.4103/wjtcm.wjtcm_67_24

[23] R. Kheirbakhsh, M. Chinisaz, S. Amanpour, S. Amini, S. Khodayari, H. Khodayari, A. Dilmaghanian, M. Haddadi, A. Ebrahim-Habibi. Turmeric effect on subcutaneous insulin-induced amyloid mass: An in vivo study. *Drug and Chemical Toxicology* **40** (2017) 1-6. https://doi.org/10.3109/01480545.2016.1163575

[24] M. Chinisaz, A. Ebrahim-Habibi, P. Yaghmaei, K. Parivar, A.-R. Dehpour. Generating local amyloidosis in mice by the subcutaneous injection of human insulin amyloid fibrils. *Experimental and Therapeutic Medicine* **8** (2014) 405-408. https://doi.org/10.3892/etm.2014.1772

[25] S.K. Metkar, A. Girigoswami, R. Vijayashree, K. Girigoswami. Attenuation of subcutaneous insulin induced amyloid mass in vivo using Lumbrokinase and Serratiopeptidase. *International Journal of Biological Macromolecules* **163** (2020) 128-134. https://doi.org/10.1016/j.ijbiomac.2020.06.256

[26] A.N. Syad, K.P. Devi. Assessment of anti-amyloidogenic activity of marine red alga G. acerosa against Alzheimer's beta-amyloid peptide 25-35. *Neurological Research* **37** (2015) 14-22. https://doi.org/10.1179/1743132814Y.0000000422

[27] Geeva, S. Narayan. Insight into the preparation of biopolymeric nanoparticles with lithium and their cellular uptake studies using PC 12 cells. *Materials Research Innovations* **26** (2022) 415-426. https://doi.org/10.1080/14328917.2021.2023288

[28] K. Harini, S.Y. Alomar, M. Vajagathali, S. Manoharadas, A. Thirumalai, K. Girigoswami, A. Girigoswami. Niosomal Bupropion: Exploring Therapeutic Frontiers through Behavioral Profiling. *Pharmaceuticals* **17** (2024) 366. https://doi.org/10.3390/ph17030366

[29] V. Kiran, K. Harini, A. Thirumalai, K. Girigoswami, A. Girigoswami. Nanotechnology's role in ensuring food safety and security. *Biocatalysis and Agricultural Biotechnology* **58** (2024) 103220. https://doi.org/10.1016/j.bcab.2024.103220

[30] S.W. Vedakumari, P. Prabu, S.J.V. Jancy, Y.R. Pravin, K. Manickavasagam, T.P. Sastry. Radiopaque fibrin nanocomplex as a promising tool for X-ray imaging applications. *International Journal of Biological Macromolecules* **200** (2022) 285-292. https://doi.org/10.1016/j.ijbiomac.2021.12.164

[31] H.S. Panda, M.D. Dhokne, S. Thakur, N. Singh, A.K. Datusalia, J.J. Panda. BDNF Loaded Amino Acid-Catecholamine Hybrid Nanoparticles as Curative Agents Against Cognitive Decline in Alzheimer's Disease. *Small* **21** (2025) 2411701. https://doi.org/10.1002/smll.202411701

[32] L. Liu, H. He, B. Du, Y. He. Nanoscale drug formulations for the treatment of Alzheimer's disease progression. *RSC Advances* **15** (2025) 4031-4078. https://doi.org/10.1039/D4RA08128E

[33] S.S.S.J. Ahmed, K. Pallavi, P.S. Aiswarya, V. Ramakrishnan, R.S.A. Husain, *Neuroprotective Compounds from Marine Microorganisms*, in *Encyclopedia of Marine Biotechnology*,2020, p. 1559-1579 9781119143802. https://doi.org/10.1002/9781119143802.ch66

[34] D. Huang, Q. Wang, Y. Cao, H. Yang, M. Li, F. Wu, Y. Zhang, G. Chen, Q. Wang. Multiscale NIR-II Imaging-Guided Brain-Targeted Drug Delivery Using Engineered Cell Membrane Nanoformulation for Alzheimer's Disease Therapy. *ACS Nano* **17** (2023) 5033-5046. https://doi.org/10.1021/acsnano.2c12840

[35] S. Udayakumar, S.K. Metkar, K. Girigoswami, A. Girigoswami. Potential effect of nanoformulated iota carrageenan in Aβ1-42 disaggregation: an in vitro, in vivo and in silico study. *ADMET and DMPK* **14** (2026) 3122. https://doi.org/10.5599/admet.3122

[36] S. Udayakumar, S.K. Metkar, A. Girigoswami, B. Deepika, G. Janani, L. Kanakaraj, K. Girigoswami. Exploring the amyloid degradation potential of nanoformulated carrageenan-bridging in vitro and in vivo perspectives. *International Journal of Biological Macromolecules* **279** (2024) 134814. https://doi.org/10.1016/j.ijbiomac.2024.134814

[37] S.K. Metkar, A. Girigoswami, R. Murugesan, K. Girigoswami. In vitro and in vivo insulin amyloid degradation mediated by Serratiopeptidase. *Materials Science and Engineering: C* **70** (2017) 728-735. https://doi.org/10.1016/j.msec.2016.09.049

[38] B. Deepika, P. Pallavi, P. Gowtham, A. Girigoswami, K. Girigoswami. Anticancer potential of nanoformulated extract of Passiflora incarnata leaves. *Biocatalysis and Agricultural Biotechnology* **57** (2024) 103109. https://doi.org/10.1016/j.bcab.2024.103109

[39] T. Nagase, K. Iwaya, T. Zako, M. Kikuchi, Y. Katsura. Insulin-derived amyloidosis (insulin ball) and skin-related complications of insulin therapy. *Nihon Yakurigaku Zasshi. Folia Pharmacologica Japonica* **158** (2023) 173-177. https://doi.org/10.1254/fpj.22109

[40] A. Dubernet, M. Toulmonde, M. Colombat, C. Hartog, E. Riviere. Insulin amyloidosis: A case report. *Frontiers in Medicine* **10** (2023) 1064832. https://doi.org/10.3389/fmed.2023.1064832.

[41] V.S. Srivatsa, R.P. Parameswari, A. Roy. Evaluation of the Antioxidant and Anti-Alzheimer's Activity of Oleanolic Acid: An In-vitro Study. *Journal of Clinical & Diagnostic Research* **19** (2025) 1. https://doi.org/10.7860/JCDR/2025/76186.20691

[42] T. Zhang, X. Wu, H. Yuan, S. Huang, S. Park. Mitigation of Memory Impairment with Fermented Fucoidan and λ-Carrageenan Supplementation through Modulating the Gut Microbiota and Their Metagenome Function in Hippocampal Amyloid-β Infused Rats. *Cells* **11** (2022) 2301. https://doi.org/10.3390/cells11152301

[43] H. Sun, L. Xu, K. Wang, Y. Li, T. Bai, S. Dong, H. Wu, Z. Yao. κ-Carrageenan Oligosaccharides Protect Nerves by Regulating Microglial Autophagy in Alzheimer's Disease. *ACS Chemical Neuroscience* **14** (2023) 3540-3550. https://doi.org/10.1021/acschemneuro.3c00460

[44] K. Kamburova, I.L. Dimitrov, F. Hodzhaoglu, V. Milkova. Investigation of the Aggregation of Aβ Peptide (1-40) in the Presence of κ-Carrageenan-Stabilised Liposomes Loaded with Homotaurine. *Molecules* **29** (2024) 3460. https://doi.org/10.3390/molecules29153460